



Recent progress in synchrotron-based frequency-domain Fourier-transform THz-EPR



Joscha Nehr Korn^{a,b}, Karsten Holldack^c, Robert Bittl^d, Alexander Schnegg^{a,*}

^a Berlin Joint EPR Lab, Institute for Nanospectroscopy, Helmholtz-Zentrum Berlin für Materialien und Energie, Kekuléstraße 5, 12489 Berlin, Germany

^b Department of Chemistry, Box 351700, University of Washington, Seattle, WA 98195, United States

^c Institute Methods and Instrumentation for Synchrotron Radiation Research, Helmholtz-Zentrum Berlin für Materialien und Energie, Albert-Einstein-Straße 15, 12489 Berlin, Germany

^d Berlin Joint EPR Lab, Fachbereich Physik, Freie Universität Berlin, Arnimallee 14, 14195 Berlin, Germany

ARTICLE INFO

Article history:

Received 11 January 2017

Revised 30 March 2017

Accepted 1 April 2017

Keywords:

Frequency-domain EPR spectroscopy

Zero-field splitting

High-spin transition-metal ion

ABSTRACT

We describe frequency-domain Fourier-transform THz-EPR as a method to assign spin-coupling parameters of high-spin ($S > 1/2$) systems with very large zero-field splittings. The instrumental foundations of synchrotron-based FD-FT THz-EPR are presented, alongside with a discussion of frequency-domain EPR simulation routines. The capabilities of this approach is demonstrated for selected mono- and multinuclear HS systems. Finally, we discuss remaining challenges and give an outlook on the future prospects of the technique.

© 2017 Elsevier Inc. All rights reserved.

1. Introduction

The detection of high-spin (HS) states and the extraction of their spin-Hamiltonian (SH) parameters is one of the major drivers behind the development of EPR spectrometers operating at increasingly higher excitation frequencies and fields. For HS transition-metal ions (TMI) and lanthanides with several unpaired electrons, spin-orbit and spin-spin interactions among unpaired electrons can induce zero-field splitting (ZFS) of the magnetic sublevels [1]. Interest in ZFS is mainly triggered by two reasons. First, it is a sensitive probe of the metal ion's coordination environment and the electronic structure [2]. ZFS values precisely determined by EPR can be used as benchmarks for state-of-the-art quantum-chemical calculations to provide insight in the relationship between electronic and geometric structure and their influence on chemical and magnetic properties [2,3]. Thus, ZFS can provide crucial details about the structure-function relationship of HS states, in *e.g.*, proteins or synthetic catalytic complexes.

Secondly, ZFS determines the magnetic properties of molecular nanomagnets (MNM). This fascinating class of compounds features a multitude of different magnetic characteristics as, for example, magnetic refrigeration [4] or single-molecule magnet (SMM) behavior [5]. The latter requires large axial ZFS, while the former favors vanishing ZFS.

The method of choice for studies in the SH parameters of paramagnetic states is EPR. However, for HS states with large ZFS, assignment and even detection of EPR transitions can be challenging. These challenges arise from the fact that ZFS can cover an energy range of several orders of magnitude well above 100 cm^{-1} (several THz) [6,7]. It can therefore induce spin-energy-level splittings far beyond the excitation-energy range of conventional single-frequency EPR spectrometers.

For half-integer (Kramers) HS systems, usually some transitions can be excited even by X- or Q-band EPR; but, for HS systems with very large ZFS, EPR transitions spread over a very broad magnetic-field/transition-energy range. The detection of only a few transitions can significantly complicate the assignment of SH parameters and ZFS in particular.

The situation is even more complicated in the case of integer-spin (non-Kramers) states (*e.g.*, Mn^{III} or Fe^{II}), where ground-state spin energy-level splittings may exceed the excitation-energy range of X- or Q-band and even single-high-frequency EPR (SHF-EPR) spectrometers. Therefore, these cases were classified as “EPR silent” in former days.

To improve this situation, for both Kramers and non-Kramers states, wide resonance-frequency (hundreds of GHz or even THz) and/or field scans (up to tens of tesla) are required. Since EPR transitions of HS systems with large ZFS are usually not known beforehand, an ideal spectrometer would enable tuning capabilities in magnetic-field- and frequency-domain, including frequency scans at zero magnetic field.

* Corresponding author.

E-mail address: alexander.schnegg@helmholtz-berlin.de (A. Schnegg).

This is the situation in FD-FT THz-EPR, which can monitor frequency-domain EPR (FD-EPR) from the microwave (MW) up to the far infrared (FIR) range. First reports about FD-FT THz-EPR date back to the 1960s [8–13]. Based on the combination of Fourier-transform infrared (FTIR) spectrometers, superconducting magnets and ultra-sensitive bolometer detectors, these early studies revealed unique insight in the ZFS of HS TMI [8–10], TMI-doped solid-state samples [11], Dy, Er and Sm ethyl sulphate [13] and even metalloproteins [10,12]. Since then, FD-FT THz-EPR has been employed for the determination of ZFS, which are too large to be studied by other EPR methods [14,15]. In spite of impressive results obtained, FD-FT THz-EPR was often limited by the low power levels available from broadband sources in the spectral range below 20 cm^{-1} (600 GHz). A team led by László Mihály improved this situation by the employment of broadband incoherent radiation, extracted from the National Synchrotron Light Source (NSLS, Brookhaven, NY, USA) [16–18]. The potential of synchrotron-based FD-FT THz-EPR, further increased drastically, when scientists at BESSY II realized a novel electron-optical mode (low α mode) [19], optimized for the generation of intense THz coherent synchrotron radiation (THz-CSR). This radiation covers the spectral window from 5 cm^{-1} to 50 cm^{-1} (150 GHz to 1.5 THz) with power levels up to three orders of magnitude higher than alternative broadband sources like incoherent synchrotron radiation or Hg-arc lamps [20]. Based on these achievements, we recently set up a dedicated FD-FT THz-EPR end-station at BESSY II [21,22] and applied it successfully to different mononuclear [23–27] and exchange coupled multinuclear HS systems [21,28–31].

In the following, we describe the working principles of synchrotron-based FD-FT THz-EPR and outline the construction

details of the FD-FT THz-EPR set-up at the electron-storage ring BESSY II. We describe FD-EPR simulation functionalities recently introduced in *EasySpin* [25,32]. The capabilities of FD-FT THz-EPR are further demonstrated by recent studies in selected mononuclear and multinuclear HS complexes. Finally, we compare FD-FT THz-EPR to other EPR concepts, discuss remaining challenges of these concepts for studies in HS systems with very large ZFS and give an outlook on the future prospects of FD-FT THz-EPR.

2. FD-FT THz-EPR detection

In contrast to conventional single-frequency EPR, FD-FT THz-EPR employs a broadband excitation source to excite the whole spectrum at once. To yield the frequency-axis, a Michelson- or Martin-Puplett interferometer (see Fig. 2) is used. Hg-arc lamps emitting in the FIR proved to be a suitable source for FD-FT THz-EPR, but their emitted intensity drastically drops below $\sim 20\text{ cm}^{-1}$. FD-FT THz-EPR down to 5 cm^{-1} comes into reach by the employment of THz-CSR as high-power broadband radiation source [21]. The maximum accessible frequency range is directly determined by the emission spectrum of the source, while the spectral resolution is the inverse of the path difference of the movable mirror in the interferometer. FD-FT THz-EPR targets optimum frequency tunability and is thus performed without resonant cavity. After passing the sample, which is mounted in a magnet or sample cryostat, time-dependent changes of the radiation are detected as a function of the mirror position in the interferometer. This transient signal is converted to frequency domain by fast Fourier transform (FFT). As detectors, liquid-He-cooled Si and InSb bolometers are ideally suited due to their superior sensitivity and dynamic range. InSb bolometers are best suited for fast lock-in

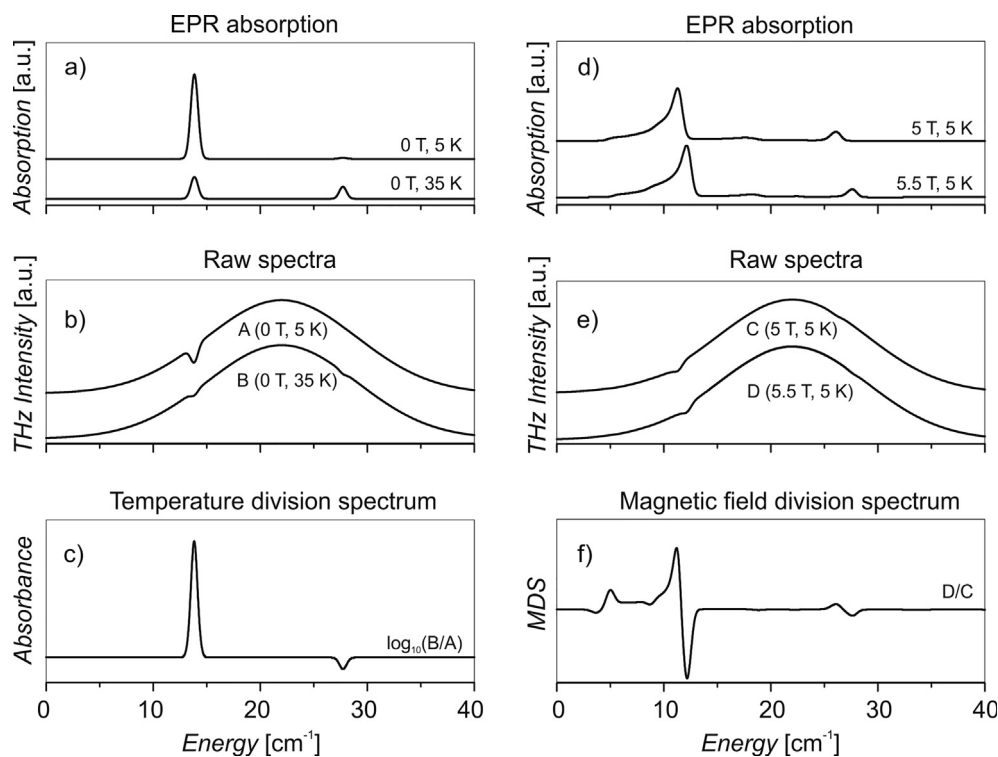


Fig. 1. Simulated FD-FT THz-EPR spectra obtained for different temperatures (left column) and magnetic fields (right column). (a) and (d) show EPR absorption spectra calculated with *EasySpin* [25,32] for $S = 5/2$, $g_{\perp} = 1.95$, $g_{\parallel} = 2.05$, $D = 6.93\text{ cm}^{-1}$ and $E = 0$ and the indicated temperatures and fields. The SH parameters correspond to Fe^{III} in hemin [25] (see Fig. 4 for an energy-level scheme and experimental FD-FT THz-EPR spectra of hemin). To demonstrate, how FD-FT THz-EPR spectra are obtained from raw spectra, EPR absorption spectra depicted in panel (a) and (d) were subtracted from a broad non-resonant background modelled by a Gaussian function. The resulting traces are depicted in panel (b) and (e), respectively. From these traces (c) the FD-FT THz-EPR absorbance spectrum $A = \log_{10}(I_{35K}/I_{5K}) = \log_{10}(B/A)$ and (f) its magnetic-field division (MDS) counterpart D/C are obtained.

detection [21] because of their large detection bandwidth (~ 1 MHz as compared to a few hundred Hz for their Si counterparts), but superfluid-He-cooled bolometers show the highest sensitivity [11]. EPR-induced transmission or reflection changes are obtained as the ratio of two raw spectra taken at different temperatures or external magnetic fields. Fig. 1 schematically depicts this procedure.

2.1. The FD-FT THz-EPR setup at BESSY II

Fig. 2 depicts the FD-FT THz-EPR user facility at the electron-storage ring BESSY II [21,22]. The spectrometer employs intense linearly polarized broadband THz-CSR as radiation source. To reduce standing waves in the spectrometer, and at the same time conserve the polarization of the excitation beam, quasi-optical elements [33] are inserted in the beamline. The THz beam extracted from the storage ring (depicted as green trace) is focused on the external radiation port of a high-resolution Michelson FTIR spectrometer (Bruker IFS 125, max. resolution: 0.0063 cm^{-1} or 200 MHz). Inside the FTIR spectrometer, THz radiation can be directed to a liquid-He-cooled sample cryostat ($T = 4.5\text{--}300\text{ K}$, Bruker Optistat), which is attached to the sample compartment for zero-field FD-FT THz-EPR (blue trace) or coupled into a quasi-optical transmission line leaving the spectrometer (green trace). This line directs the radiation to an optical bench. On it, the radiation can again be switched to two different pathways through a superconducting split coil magnet. The magnet contains a variable-temperature insert (VTI) equipped with four THz-transparent z-cut quartz windows. The propagation direction of the THz radiation is defined by the vector \mathbf{k} . Its orthogonal pathways through the magnet correspond to Faraday (green trace, $\mathbf{B}_0 \parallel \mathbf{k}$) and Voigt (red trace, $\mathbf{B}_0 \perp \mathbf{k}$) configurations. In Voigt geometry, the polarization of the linearly polarized THz light can be

rotated around the \mathbf{k} -vector by a broadband rooftop-mirror polarization shifter [34] (see photo (a) in Fig. 2).

The magnet allows for measurements from $T = 1.5\text{ K}$ to 300 K , at external magnetic fields variable between -10 and $+10\text{ T}$ ($\pm 11\text{ T}$ with pumped He reservoir). The option to apply positive and negative magnetic fields provides additional important experimental capabilities in frequency-domain EPR. It allows for, e.g., real time monitoring of quantum tunneling of SMMs [35].

Due to the typically broad inhomogeneous line widths of HS systems with large ZFS, FD-FT THz-EPR can be performed with high-field magnets providing field homogeneities in the per mille range. For the present set-up, excellent results on HS TMI could be obtained with field homogeneities of 0.6% in a 10 mm diameter sphere [21,23–31].

For EPR measurements in the range between 5 cm^{-1} and 50 cm^{-1} optimum conditions are achieved with THz-CSR. For higher excitation energies, the internal Hg-arc lamp of the FTIR spectrometer provides sufficient radiation power. The upper excitation-energy limit is mainly determined by the employed window materials (typically Mylar, quartz or diamond). If the sample is mounted in the magnet cryostat this limit is 180 cm^{-1} , even higher excitation energies are achievable in the cryostat without field coils.

In both configurations, highly sensitive detection can be achieved with Si-bolometers (IR labs, cooled to 4.2 K or 1.6 K), an InSb bolometer (QMC, cooled to 4.2 K) or a fast Schottky-diode THz detector (ACST, RT; $<250\text{ ps}$ time resolution). The signal from the THz-diode detector can be further amplified by a 600-MHz lock-in detector (UHFLI Zurich Instruments™) locked to the 500-MHz repetition rate of the THz-pulses emitted by the storage-ring. The depicted FD-FT THz-EPR set-up is part of the HZB user program and can be accessed via the online-access tool Gate [36].

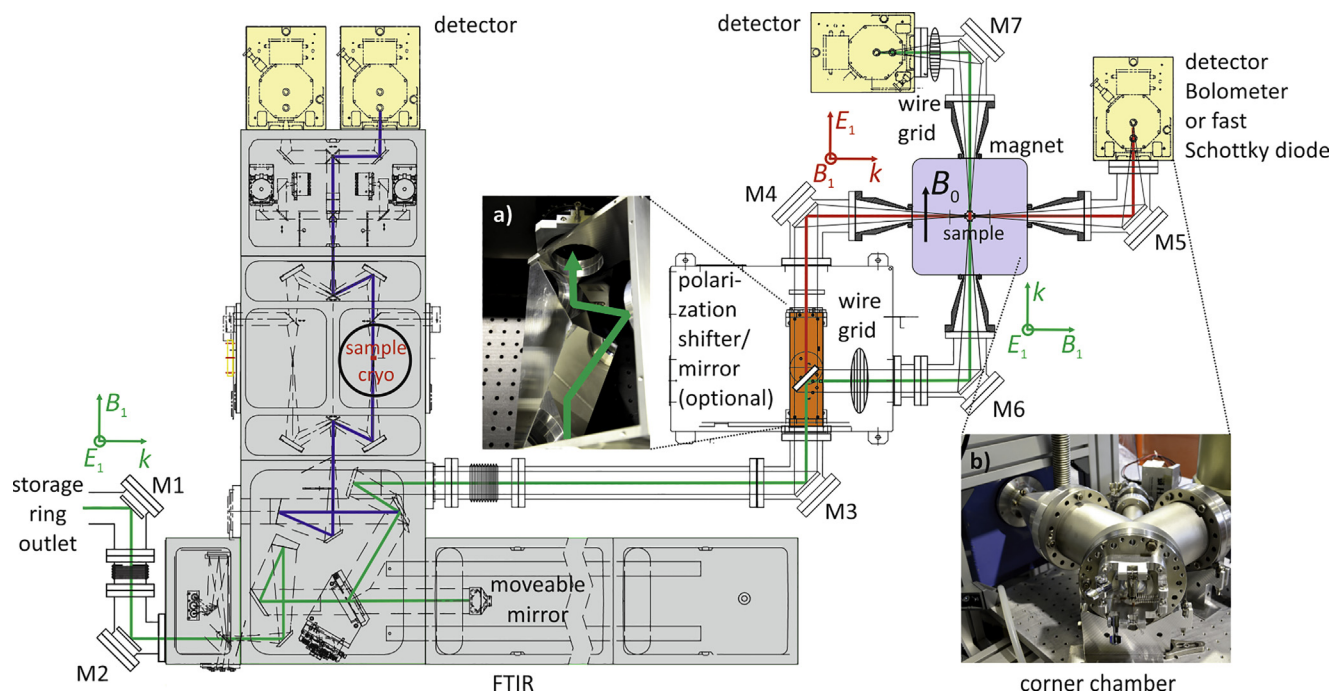


Fig. 2. Scheme of the FD-FT THz-EPR spectrometer with FTIR spectrometer (gray), polarization shifter (orange), sample magnet (light blue) and detectors (yellow). THz radiation is transmitted by a quasi-optical beamline through either the sample cryostat (dark blue trace) or the sample magnet in Faraday (green trace) or Voigt geometry (red trace). Green and red coordinate systems indicate the orientation of the electric- and magnetic-field components as well as the propagation direction of the THz-radiation, \mathbf{E}_1 , \mathbf{B}_1 and \mathbf{k} , respectively. Photos (a) and (b) depict the polarization rotator with the THz beam pictured in green and the last vacuum corner chamber connecting magnet and bolometer, respectively. Corner chambers M4 to M7 accommodate off-axis quasi-optical mirrors, which can be adjusted from outside by the mechanical mechanism shown in the photograph. (For interpretation of the references to color in this figure legend, the reader is referred to the web version of this article.)

3. FD-EPR simulations

Broadband FD-FT THz-EPR in the optimum case allows for the extraction of ZFS directly from the zero-field spectrum, which constitutes one of the most apparent benefits of this approach. However, for a precise determination of SH parameters and the interpretation of FD-EPR spectra in the presence of an external magnetic field, computer simulations are necessary. Field- and frequency-domain EPR are complementary. Nevertheless, a tool for simulations of both modalities with the same SH model became available only recently and is therefore outlined in the following.

For a complex containing several electron spins with quenched orbital angular momentum coupled to each other and the surrounding nuclei, the SH is written:

$$\hat{H}_{\text{cluster}} = \hat{H}_{\text{Zee}} + \hat{H}_{\text{ZFS}} + \hat{H}_{\text{SS}} + \hat{H}_{\text{Nuc}} \quad (1)$$

In this equation, \hat{H}_{Zee} accounts for the Zeeman interaction, \hat{H}_{ZFS} for the ZFS and \hat{H}_{SS} for the spin-spin couplings of the electron spins. \hat{H}_{Nuc} finally collects hyperfine and nuclear quadrupole interactions.

Field-domain EPR calculations based on Eq. (1) are carried out with different simulation programs. The most complete and versatile numerical EPR package currently available is *EasySpin* [32], written and maintained by Stefan Stoll (University of Washington, Seattle, WA, USA).

In spite of the similarity in the approach, FD-EPR simulations are computationally less expensive since they require only one diagonalization to calculate the whole spectrum, whereas field-domain simulations require several diagonalizations and the use of advanced interpolation schemes. However, for the calculation of FD-EPR spectra, a program with versatility and accessibility, comparable to field-domain simulation programs, was missing until recently. Furthermore, existing simulation programs were limited to the calculation of EPR spectra for MW magnetic fields, \mathbf{B}_1 , linearly polarized either perpendicular or parallel to \mathbf{B}_0 . This situation corresponds to the boundary conditions imposed by the employment of wave guides and MW resonators. Though, FD-FT THz-EPR and other high-frequency/high-field EPR approaches involve MW beams with circular polarization [37], unpolarized radiation [38] or non-orthogonal field geometries [27]. These cases are not covered by the standard continuous-wave EPR (CW EPR) transition probabilities implemented in most EPR-simulation programs. To bridge this gap and increase the versatility of simulation

capabilities to these new situations, we derived novel general and compact closed-form expressions for calculating magnetic-transition dipole moments and transition rates in solid-state EPR experiments on crystals and disordered materials. These expressions are valid for arbitrary spin centers and arbitrary excitation geometries (Faraday, Voigt, intermediate). They cover resonator setups and beam experiments with unpolarized excitation, linear polarization and circular polarization. Equations corresponding to these cases can be found in Ref. [27] and are implemented in *EasySpin* for field- and frequency-domain CW-EPR simulations.

Based on the derived representation-free expression for transition probabilities, a fully flexible FD-EPR simulation option was integrated into *EasySpin* [25,27]. Fig. 3 and 4 demonstrate the possibility to reproduce both resonance positions and intensities of experimental FD-FT THz-EPR spectra over a very broad excitation-frequency/magnetic-field range for different alignments of \mathbf{B}_1 and \mathbf{B}_0 . The new simulation capabilities now allow for the calculation of frequency- and field-domain EPR spectra with the same variety of SH parameters, line-shape models, least-square fitting abilities and EPR-excitation geometries with one simulation program [27].

4. FD-FT THz-EPR applications

In this section we exemplify the application range of FD-FT THz-EPR for a few selected half-integer and integer mononuclear HS TMs as well as exchange-coupled multinuclear HS clusters.

4.1. Mononuclear HS systems

The magnetic properties of mononuclear HS systems can be described by the following SH:

$$\hat{H} = \hat{H}_{\text{Zee}} + \hat{H}_{\text{ZFS}} \quad (2)$$

$$\hat{H}_{\text{Zee}} = \mu_B \hat{\mathbf{S}} \mathbf{g} \mathbf{B}_0 \quad (3)$$

$$\hat{H}_{\text{ZFS}} = \hat{\mathbf{S}} \mathbf{D} \hat{\mathbf{S}} \quad (4)$$

where \hat{H}_{Zee} denotes the electron Zeeman interaction of the electron-spin vector, $\hat{\mathbf{S}}$ with \mathbf{B}_0 , μ_B is the Bohr magneton and \mathbf{g} the electron g -tensor. \hat{H}_{ZFS} contains the ZFS, with \mathbf{D} being the ZFS -tensor. In the ZFS-tensor frame, \mathbf{D} is diagonal and the element with the strongest magnitude is D_{zz} , such that $\mathbf{D} = \text{diag}(-\frac{1}{3}D + E, -\frac{1}{3}D - E, \frac{2}{3}D)$ with

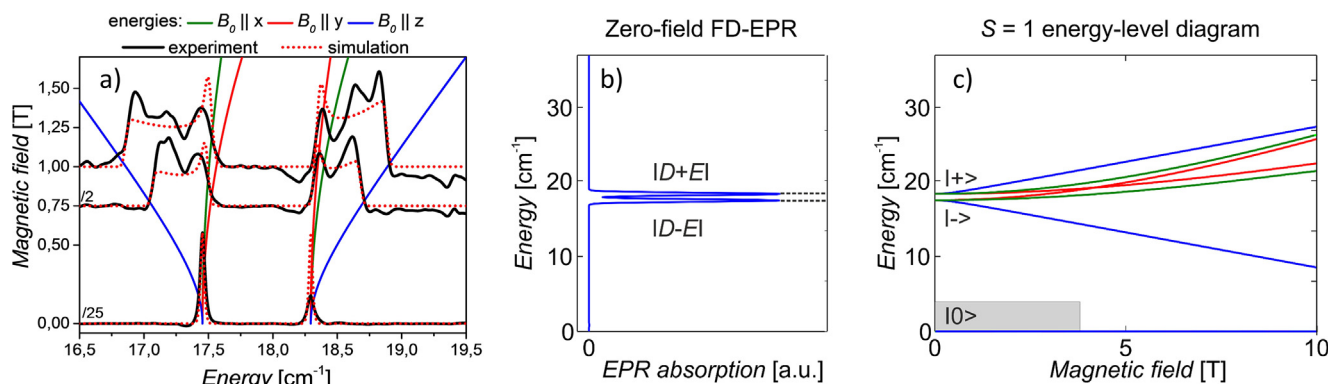


Fig. 3. (a) Experimental (solid black) and simulated (red dotted) field-dependent FD-FT THz-EPR absorbance spectra of $[\text{Tp}_2\text{Mn}]\text{SbF}_6$ ($S = 1$). Experimental spectra were obtained at the indicated magnetic fields by dividing raw spectra taken at 40 K and 2 K. Spectra taken at 0 and 0.75 T are divided by 25 and 2, respectively. Adapted with permission from Nehr Korn, et al. J. Phys. Chem. B, 119 (2015) 13816. Copyright 2017 American Chemical Society. (b) Simulated zero-field FD-EPR spectrum depicted in (a) plotted for a broader transition energy range. (c) Spin-energy levels for the same SH parameters depicted for $\mathbf{B}_0 \parallel x$ (green), $\mathbf{B}_0 \parallel y$ (red) and $\mathbf{B}_0 \parallel z$ (blue). Energy levels are normalized to the ground state, i.e., the energy difference to this state is plotted. The gray box indicates the spectral range accessible to conventional EPR spectrometers. For further details, see Refs. [23,25]. (For interpretation of the references to color in this figure legend, the reader is referred to the web version of this article.)

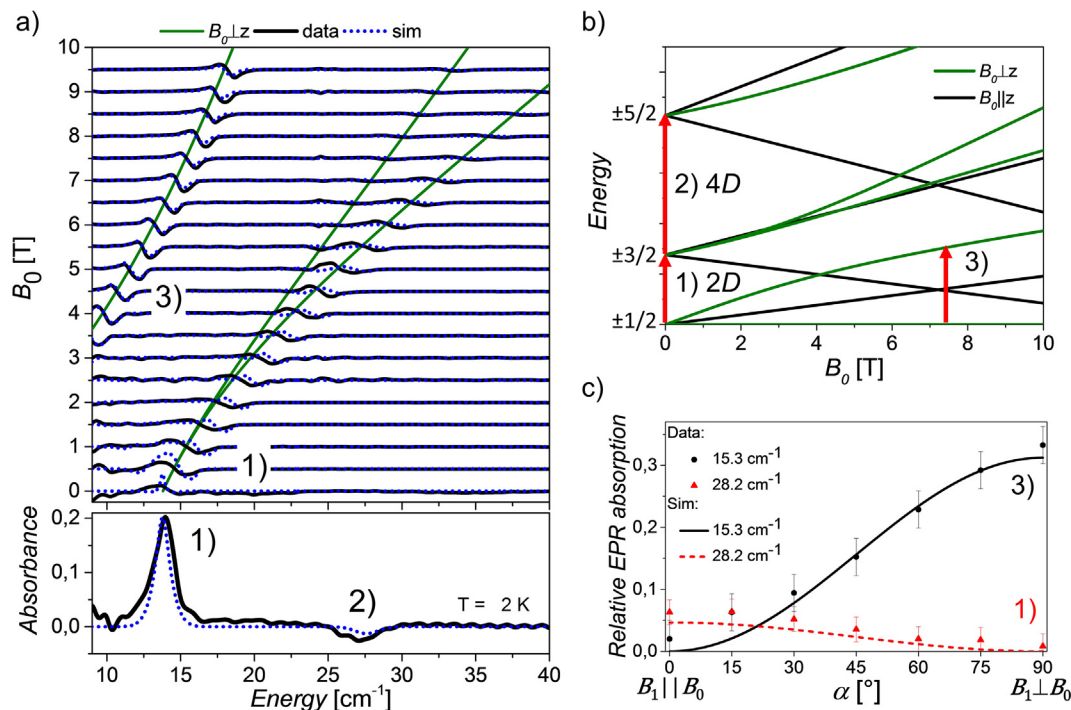


Fig. 4. FD-FT THz-EPR of hemin in Fe^{III} ($S = 5/2$) state. (a) Experimental (black solid lines) and simulated (blue dotted lines) spectra. The upper panel depicts MDS spectra, while the lower panel shows a zero-field FD-FT THz-EPR absorbance spectrum obtained by dividing raw spectra taken at 40 K and 2 K. Simulated ground-state transition energies for $B_0 \parallel z$ (green lines) are shown in the upper panel. Data are offset for clarity. For further details see Ref. [25]. Adapted with permission from Nehrkorn, et al. J. Phys. Chem. B, 119 (2015) 13816. Copyright 2017 American Chemical Society. (b) Corresponding spin-energy level diagram with M_S quantum numbers plotted along the y-axis. Energy levels are normalized to the ground state. EPR transitions (1) to (3) depicted in (a) are highlighted by red arrows. (c) Dependence of EPR transitions (1) (red triangles) and (3) (black circles) on the angle α between B_1 and B_0 , measured at $B_0 = 7.5$ T and $T = 2$ K. Corresponding simulations are shown as red dotted and black solid lines, respectively. For further details, see Refs. [25,27]. Adapted with permission from Nehrkorn et al. Phys. Rev. Lett., 114 (2015) 010801. Copyright 2017 American Physical Society. (For interpretation of the references to color in this figure legend, the reader is referred to the web version of this article.)

the axial and rhombic ZFS parameters D and E , respectively. Under the assumption of purely axial ZFS, and in zero field, the spin-energy levels are split in doublets according to the magnitude of the M_S quantum number (M_S being the eigenvalue of the operator \hat{S}_z). The only exception is the $M_S = 0$ state, which is a singlet when present. For integer HS systems, the degeneracy is lifted by the rhombic ZFS parameter E . By contrast, half-integer HS systems remain degenerate at zero field, no matter which term is added to the SH. As a result, half-integer and integer-spin systems differ in their EPR properties. The consequences of this fact are exemplified for integer ($S = 1$) and half integer ($S = 5/2$) systems exhibiting very large ZFS.

4.1.1. FD-FT THz-EPR of [Tp₂Mn]SbF₆ (Mn^{III}, $S = 1$)

Fig. 3(a) depicts FD-FT THz-EPR absorbance spectra of [Tp₂Mn]SbF₆ containing Mn^{III} in $S = 1$ state. At cryogenic temperatures, two pronounced EPR resonances are observed already at zero magnetic field. These transitions can be directly assigned to transitions between the three spin states $|0\rangle$, $|+\rangle$ and $|-\rangle$ depicted in Fig. 3(c) (note that transitions between $|+\rangle$ and $|-\rangle$ are EPR forbidden). The energies of these states are $-\frac{2}{3}D, \frac{1}{3}D + E$ and $\frac{1}{3}D - E$, respectively. Hence, D and E can be accurately determined from the zero-field spectrum. This is an important advantage over X-, Q- or even W-band single-frequency EPR, which would fail to detect any ground-state EPR transition for the given case (see gray box in Fig. 3(c)). Even SHF-EPR operating below 510 GHz (17 cm⁻¹) would only excite a small part of the spectrum. However, results complementary to FD-EPR can be obtained by multi-high frequency EPR (MHF-EPR) employing multiple radiation sources and broad magnetic-field scans [23]. Ultimate robustness and accuracy in the SH parameters of HS systems can be attained by combined

MHF- and FD-EPR studies. In the present case, both ZFS- ($D = 17.87$ cm⁻¹ and $E = 0.42$ cm⁻¹) and g -values ($g_x = 2.065$, $g_y = 2.073$, $g_z = 1.978$) could be determined with high precision by the combination of FD-FT THz-EPR and ultra-wide band MHF-EPR [23,25].

4.1.2. FD-FT THz-EPR of ferric ($S = 5/2$) hemin

Fig. 4 depicts FD-FT THz-EPR spectra of the ferric iron ($S = 5/2$) in hemin (Fe(PPIX)Cl, chloro[3,7,12,17-tetramethyl-8,13-divinylporphyrin-2,18-dipropionato(2-)]Fe^{III}). Experimental spectra were obtained on powder samples that were mixed with high-density polyethylene, (HDPE) finely ground and pressed to a pellet. The lower panel in Fig. 4(a) shows the zero-field absorbance spectrum. Two EPR transitions with opposite sign are clearly identified. Positive and negative contributions to the FD-FT THz-EPR spectrum originate from the division by reference spectra. Ground state transitions exhibit the largest population difference and hence strongest EPR at very low temperatures. At higher temperatures, where reference spectra are taken, the intensity of ground-state transitions is strongly reduced, while transitions between higher lying excited states gain in intensity.

Based on their sign and spectral position, the observed EPR peaks can be assigned to a ground-state transition and a transition between excited states. In case of vanishing rhombicity transition energies are $2D$ and $4D$, respectively. The opposite sign is a result of the division of raw spectra taken at different temperatures (see Fig. 1(b) and (c)). ZFS parameters can be directly determined from the zero-field spectrum. To determine both D and E the detection of two zero-field transitions is required. However, the detection of a ground-state EPR transition and at least one transition

between excited states is sometimes difficult, due to smaller population differences in the latter case.

Therefore, the field dependence of the ground-state EPR transitions has to be studied for a definite assignment of the ZFS parameters. According MDS FD-FT THz-EPR spectra for hemin are depicted in the upper panel of Fig. 4(a). In addition to (1), transition (3) is observed at 3.5 T and higher fields. This transition is also accessible to conventional EPR and can be used for estimates of D . Yet, much more precise SH-parameters are obtainable by a simultaneous simulation of zero-field and MDS FD-FT THz-EPR spectra, which yielded in the present case: $D = 6.930(5) \text{ cm}^{-1}$, $|\frac{E}{B}| = 0.00(2)$, $g_{\perp} = 1.95(5)$, $g_{\parallel} = 2.05(5)$ [25].

Further valuable information on the parity of the involved spin states can be obtained by measuring the dependence of the EPR transitions on the orientation between \mathbf{B}_1 and \mathbf{B}_0 . In Fig. 4(c), experimental and simulated [27] intensities of transition (1) and (3) are plotted vs. α , the angle between \mathbf{B}_1 and \mathbf{B}_0 , in Voigt configuration. Gradual change of α is not possible in conventional EPR spectrometers but, quasi-optical spectrometers, like the set-up depicted in Fig. 2, provide more experimental freedom and allow for the realization of such experiments. From Fig. 4(c), it becomes apparent that the α dependence of the two EPR transitions clearly differs.

Transition (3), which corresponds to a transition from the ground state to the first excited state, reaches its maximum for $\mathbf{B}_0 \perp \mathbf{B}_1$ and disappears for $\mathbf{B}_0 \parallel \mathbf{B}_1$. For this transition, the magnetic-dipole moment is complex, perpendicular to \mathbf{B}_0 , and has odd parity. On the contrary, transition (1), which corresponds to a transition between two states with equal parity, shows exactly opposite dependence on α . For this case the magnetic-dipole moment is real and parallel to \mathbf{B}_0 [27]. This assignment is quantitatively confirmed by simulations, that have been obtained with *EasySpin* based on equations published in Ref. [27]. Such EPR linear dichroism experiments can be used to determine parities of states involved in EPR transitions. This information is of great relevance in, e.g., SMM research, where parity impacts quantum tunneling effects.

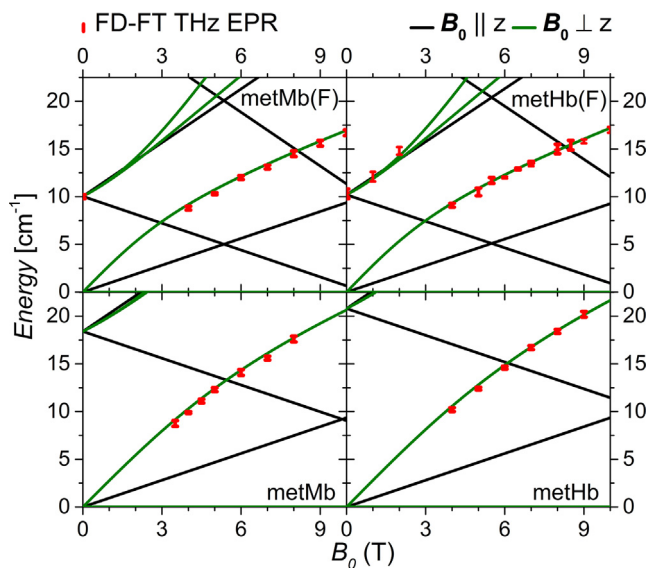


Fig. 5. FD-FT THz-EPR transitions (red symbols) for metMb (left) and metHb (right), both with fluoro (top) and aquo (bottom) ligands. Experimental results are plotted together with the lowest energy levels calculated for $\mathbf{B}_0 \parallel z$ (black lines) and $\mathbf{B}_0 \perp z$ (green lines) with Eq. (2) and SH parameters given in the text. For further details, see Ref. [24]. (For interpretation of the references to color in this figure legend, the reader is referred to the web version of this article.)

4.1.3. FD-FT THz-EPR on ferric met-hemoglobin and -myoglobin

Studies in the ZFS of HS iron porphyrins are not limited to model systems but can be even extended to metalloproteins. As an example, Fig. 5 depicts EPR resonances obtained from FD-FT THz-EPR spectra of the met states (Fe^{III} , $S = 5/2$) of hemoglobin and myoglobin, both with fluoro and aquo ligands. Measurements were performed at IHe temperatures on frozen aqueous solutions containing heme concentrations between 11(2) mM and 22(2) mM. From experimental FD-FT THz-EPR spectra, the field dependence of spin transitions within the ground-state doublet, for all four protein systems, and transitions between ground state and first excited doublet for metHb and metMb fluoro-states could be recorded. These transitions are plotted in Fig. 5 against spin-energy-levels calculated with Eq. (2). From comparison between experimental and simulated FD-FT THz-EPR data, we found purely axial ZFS of: $D = 5.0(1) \text{ cm}^{-1}$ (fluoro-metMb), $D = 9.2(4) \text{ cm}^{-1}$ (aquo-metMb), $D = 5.1(1) \text{ cm}^{-1}$ (fluoro-metHb) and $D = 10.4(2) \text{ cm}^{-1}$ (aquo-metHb).

4.2. Multinuclear HS systems

Multinuclear HS clusters with N exchange-coupled electron spins are among the major targets of EPR studies, due to their importance in (bio-)catalysis [39] and as MNMs [5]. Their SH writes:

$$\hat{H} = \sum_{i=1}^N \hat{H}_{\text{Zee},i} + \sum_{i=1}^N \hat{H}_{\text{ZFS},i} + \hat{H}_{\text{Ex}} \quad (2)$$

$$\hat{H}_{\text{Ex}} = -2 \sum_{i>j} \hat{\mathbf{S}}_i \cdot \mathbf{J}_{ij} \cdot \hat{\mathbf{S}}_j.$$

Here $\hat{H}_{\text{Zee},i}$ and $\hat{H}_{\text{ZFS},i}$ are again the single-ion Zeeman interaction and ZFS, respectively, as defined in Eq. (2). In addition, \hat{H}_{Ex} represents the exchange interaction between electron spins, where \mathbf{J}_{ij} is the exchange interaction between the i th and j th electron spin. When only \hat{H}_{Ex} is present, and \mathbf{J}_{ij} is isotropic, S is a good quantum number ($\hat{S}^2|S\rangle = S(S+1)|S\rangle$). A full magnetic characterization of an exchange coupled complex requires the determination of both, \mathbf{J}_{ij} and ZFS. The direct determination of large exchange interactions by EPR is hampered by the fact that transitions between multiplets differing in S are EPR forbidden [40]. However, such transitions can be observed by inelastic neutron scattering (INS) [41]. In principle, the INS spectra already contains all the desired information, but oftentimes the assignment of the different INS peaks is not possible or plagued with ambiguity. Due to its difference in the selection rules, complementary FD-FT THz-EPR measurements can significantly simplify this task. Beyond this, FD-FT THz-EPR provides higher sensitivity and resolution compared to INS and, such, can often be applied to cases, where INS fails.

4.2.1. The single molecule magnet $\text{Mn}_2\text{Os} \cdot 7\text{MeOH}$

The relevance of EPR for the characterization of SMM was highlighted by the early assignment of large ZFS as source of the magnetic anisotropy in the paradigm SMM Mn_{12}AC , determining the energy barrier against magnetization reversal [42]. This spectroscopic breakthrough induced intense ongoing field-domain [43,44] and frequency-domain EPR [21,31,35,45] studies in the SH parameters of SMMs. The aim of these studies is the assignment and understanding of the parameters determining the barrier against magnetization reversal and thereby pave the way for SMMs exhibiting slow relaxation of the magnetization at ever higher temperatures. In the quest for systems exhibiting larger magnetic anisotropies, much effort is devoted to 4d, 4f and 5d metal ions with unquenched orbital momentum.

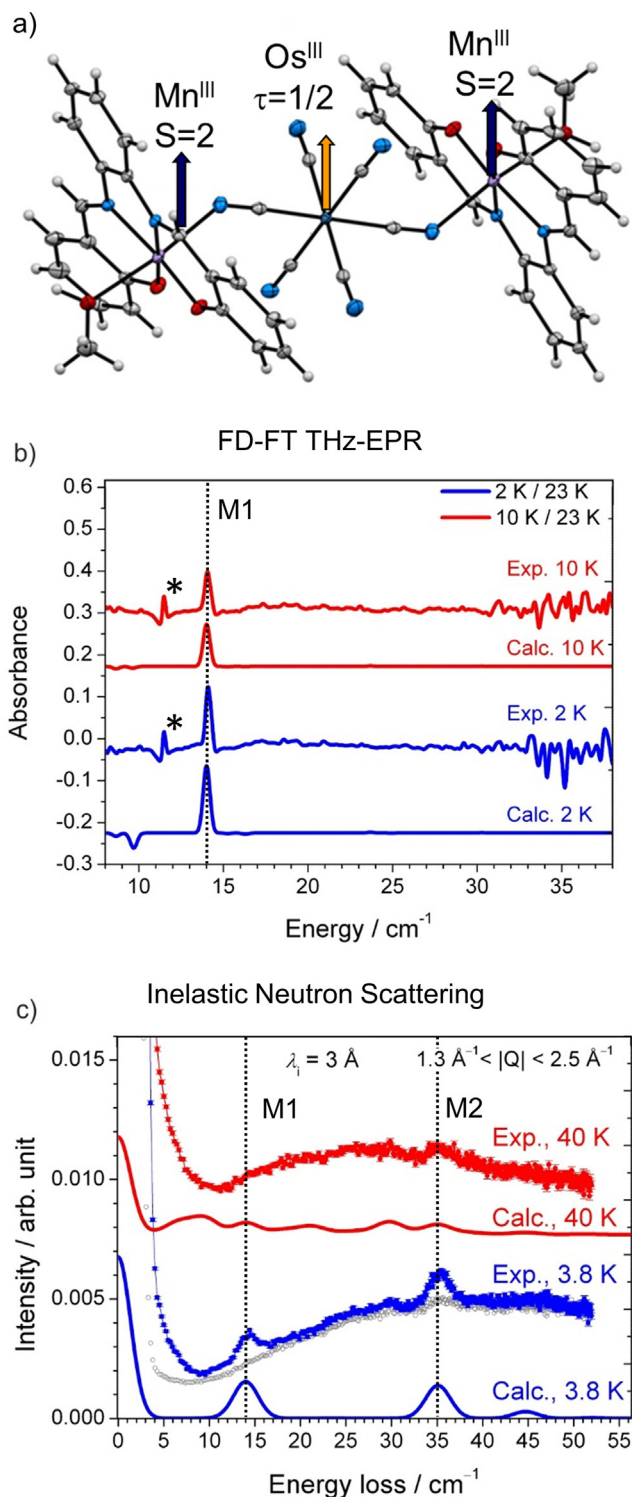


Fig. 6. (a) Molecular structure of the trinuclear Mn_2Os anion in $\text{Mn}_2\text{Os} \cdot 7\text{MeOH}$. Os - dark blue, Mn - magenta, N - blue, O - red, C - gray. Experimental (Exp.) and simulated (Calc.) FD-FT THz-EPR absorbance spectra (b) and INS spectra (c) of $\text{Mn}_2\text{Os} \cdot 7\text{MeOH}$. THz-EPR and INS spectra are recorded at zero magnetic field and at the temperatures indicated in the respective boxes. Non magnetic transitions in the FD-FT THz-EPR spectra are marked by an asterisk. λ is the incoming neutron wavelength and Q the momentum transfer to $\text{Mn}_2\text{Os} \cdot 7\text{MeOH}$. The gray line indicates the estimated phonon background, which was estimated by rescaling a high temperature spectrum (here 40 K) by the Bose factor [46]. Spectra are offset for clarity. Dotted lines indicate ground state transitions M1 and M2 identified by their magnetic field (for M1), temperature and Q dependence [31]. SH parameters of the simulations are given in the text. Adapted with permission from Pinkowicz et al. J. Am. Chem. Soc., 137 (2015) 14406. Copyright 2017 American Chemical Society.

Fig. 6(a) depicts the molecular structure of the $\{[\text{Mn}^{\text{III}}(\text{salphen})]_2 [\text{Os}^{\text{III}}(\text{CN})_6]\}$ anion in $(\text{PPN}^+)[\text{Mn}^{\text{III}}(\text{salphen})]_2 [\text{Os}^{\text{III}}(\text{CN})_6] \cdot 7\text{MeOH}$ ($\text{Mn}_2\text{Os} \cdot 7\text{MeOH}$) (PPN^+ = bis(triphenylphosphoranylidene) ammonium cation; $\text{H}_2\text{salphen}$ = N,N' -bis(salicylidene)-1,2-diaminobenzene). $\text{Mn}_2\text{Os} \cdot 7\text{MeOH}$ is a trinuclear cyanide bridged complex containing two Mn^{III} ($3d^4$) and a Os^{III} ($5d^5$). It behaves as an SMM with an effective barrier for the magnetization reversal, (U_{eff}/k_B), of 17.1 K. In Fig. 6(b) and (c) FD-FT THz-EPR and INS spectra of $\text{Mn}_2\text{Os} \cdot 7\text{MeOH}$ are plotted, respectively. In zero field, FD-FT THz-EPR spectra exhibit one ground-state transition (M1) at 14.1 cm^{-1} . The intensity of this transition decreases with increasing temperature due to a decrease of the population difference of the spin-energy levels. In addition, M1 splits in an externally applied magnetic field. INS spectra show a ground-state transition at the same spectral position. Though, in addition to M1, INS spectra contain a second ground-state transition M2 at 35 cm^{-1} with nearly the same intensity as M1. The latter peak is not observed in the FD-FT THz-EPR. These findings in combination with an analysis of the Q -dependence, allowed for an assignment of M1 to an EPR allowed transition from the spin-ground state and M2 to an INS allowed but EPR forbidden transition from the same spin state [31].

SH parameters for $\text{Mn}_2\text{Os} \cdot 7\text{MeOH}$ were obtained by fits to the experimentally obtained INS and FD-FT THz-EPR spectra and magnetometry data [31]. Os^{III} has unquenched orbital angular momentum. Its splitting between the ground state doublet and excited states exceeds 4500 cm^{-1} [47]. Hence, Os^{III} can be described by an effective spin $\tau = 1/2$ experiencing pronounced exchange interactions to each of the Mn^{III} ($S=2$). A comparison of SH models employing isotropic and anisotropic exchange interactions revealed that isotropic exchange between the metal ions is not able to reproduce the experimental data. Instead, anisotropic exchange has to be introduced to reproduce both INS and FD-FT THz-EPR data with Eq. (3), and the same set of SH parameters [31]. The Jahn-Teller axes of the Mn^{III} are identified from analysis of X-ray diffraction data and are chosen as main anisotropy axes, resulting in a tilt between molecular and ZFS frame of the Mn^{III} ions. Yet, ambiguity in the coordinate frame of the anisotropic exchange interaction remained. Three parameter sets were obtained, which fit the experimental data equally well. The corresponding parameter sets, labeled X, Y, Z, are summarized in Table 1). Simulations using Fit X are shown in Fig. 6.

The main deviation between these parameter sets is the sign of the individual J components. Nevertheless, the obtained SH parameters clearly revealed that anisotropic exchange is necessary to yield satisfactory match between calculated and experimental data. In fact, it turned out that the magnetic anisotropy of the molecule *in toto* is not due to ZFS of the incorporated TMI, but due to anisotropic exchange interactions between them [31].

These results are in accordance with previous FD-FT THz-EPR studies in the SH parameters properties of similar trinuclear $\text{Mn}^{\text{III}}\text{-M}^{\text{III}}\text{Mn}^{\text{III}}$ ($\text{M} = \text{Cr}$ ($3d$), Ru ($4d$), Os ($5d$)) complexes [28–30]. Also in $(\text{NEt}_4)[\text{Mn}^{\text{III}}(5\text{-Brsalen})]_2[(\text{MeOH})_2\text{M}^{\text{III}}(\text{CN})_6]$, with ($\text{M} = \text{Os}$ and Ru) pronounced anisotropic exchange between the ions was observed. In addition it was found that the average magnitude of the anisotropic exchange increases upon replacement of Ru by Os [30]. This fact could be rationalized by the more diffuse $5d$ orbitals

Table 1
Best-fit SH parameters for $\text{Mn}_2\text{Os} \cdot 7\text{MeOH}$ [31].

	Fit X	Fit Y	Fit Z
J_{xx}/cm^{-1}	+30.0(5)	−25.5(5)	−22.0(5)
J_{yy}/cm^{-1}	−23.5(5)	+32.0(5)	−25.9(2)
J_{zz}/cm^{-1}	−24.0(5)	−24.0(5)	+28.9(2)
$D_{\text{Mn}}/\text{cm}^{-1}$	−4.1(1)	−4.2(1)	−3.7(1)

of Os as compared to the 4d orbitals of Ru [30]. In this study, anisotropy in the exchange could be assigned to a bent geometry of the $\text{Mn}^{\text{III}}\text{M}^{\text{III}}\text{Mn}^{\text{III}}$ chain. Based on the unique information content extractable from combined FD-FT THz-EPR and INS, these important findings, further promote exchange interactions as source of magnetic anisotropy and possible lever to increase the energy barrier in SMSs.

5. Discussion

5.1. Comparison of FD-FT THz-EPR to other EPR-spectrometer concepts

FD-FT THz-EPR's main field of application is the detection of EPR resonances distributed over a broad transition-energy/magnetic-field range ($5\text{--}180\text{ cm}^{-1}/-11\text{ T}$ to 11 T). Such systems are, at least partly, also accessible to other high-field/high-frequency EPR approaches, like field-swept SHF-EPR [48], MHF-EPR [49] and frequency-domain magnetic resonance (FDMR) [35,45]. The technique most closely related to FD-FT THz-EPR is FDMR, which also provides FD-EPR spectra at fixed or zero magnetic field as absolute absorption or transmission change. In FDMR, changes of the resonance condition are achieved by sweeps of the excitation frequency. Similar results can in principle be obtained by absorption spectroscopy employing the broadband excitation spectrum of laser driven THz-sources in a THz time domain spectroscopy (THz-TDS) experiment [50,51]. Up to now, this approach found only very little application in FD-EPR spectroscopy, but may gain importance due to the rapid progress in laser-based THz spectroscopy. The performance of FDMR, FD-FT THz-EPR and THz-TDS for studies in the magnetic properties of MNMs was recently compared by van Slageren [45].

On the contrary, SHF- and MHF-EPR are field-domain EPR techniques. SHF-EPR spectrometers are optimized to a limited excitation-energy range and usually incorporate a sample resonator, while MHF-EPR spectrometers allow for excitation at many different frequencies. Comparisons of different spectrometer approaches for the detection of very large ZFS are published, e.g., in Refs. [44,45].

SHF-EPR employing resonant structures is superior to MHF- and FD-EPR with respect to its absolute sensitivity and the possibility to perform pulse and double-resonance experiments. Higher absolute sensitivities are particularly important when the sample amount is limited, like in most protein studies. Yet, for applications to HS systems with large ZFS, SHF-EPR experiences severe limitations, as it can only provide a one-dimensional scan through the two-dimensional energy-field landscape. In the worst case, it may completely miss the ZFS transitions in a given HS system. Due to this fact, ultra-broadband methods like MHF-EPR, FDMR or FD-FT THz-EPR might be the better choice to map out the spin-transition energy/field landscape for concentrated HS samples with large ZFS.

Comparing different broadband EPR methods, MHF-EPR and FDMR potentially exhibit higher spectral resolution as compared to FD-FT THz-EPR. In the latter case, the resolution is determined by the FTIR spectrometer (typically $>0.01\text{ cm}^{-1}$ or 300 MHz). It is, therefore, unsuitable for the resolution of small g -tensor anisotropies or hyperfine interactions. However, large ZFS of HS states are determined by measurements of ground-state EPR transitions, which typically exhibit inhomogeneous line widths beyond the instrumental limit.

MHF-EPR and FDMR experiments can cover a broad range of excitation energies from below 1 cm^{-1} to about 50 cm^{-1} , but 30 cm^{-1} are a more realistic limit. The extension of this range to higher energies is restricted by the lack of sources providing sufficient power. By contrast, FD-FT THz-EPR reaches much higher exci-

tation energies ($\approx 180\text{ cm}^{-1}$ for the BESSY II setup), which can be extended further towards the FIR range. This can be achieved by a proper choice of the optical components and the window materials. Further striking advantages of FD-FT THz-EPR and FDMR over field-domain EPR approaches are the capability to record zero-field EPR spectra and the possibility to compare absolute EPR intensities over a broad energy/field range. In FD-FT THz-EPR ultra-broadband measurements can be performed with a single excitation source.

5.2. Current limits of ultra-broadband EPR

Despite ongoing progress in high-field/high-frequency EPR-spectrometer technology and simulation capabilities, simulated EPR spectra of HS systems do not yet reach the excellent agreement, which is routinely achieved for X- or Q-band EPR spectra of, e.g., organic radicals. This observation is not a peculiarity of FD-EPR, but has been stated also for field-domain MHF-EPR [49,52]. Deviations between experimental and simulated spectra may be due to sample-related, computational and instrumental reasons. In the following, we summarize some of the issues that can lead to uncertainties in the interpretation of HS systems with large ZFS and discuss possible measures to improve the situation.

In general, sample morphology, concentration and solvent effects impact the EPR spectrum. In conventional EPR, it is common practice to measure diluted samples (μM and below) as frozen solutions in solvents that form good glasses. Thereby, excellent powder patterns are obtained and inter-molecular spin couplings are suppressed. Due to sensitivity limitations and strong dielectric absorption of most solvents in the THz-range, this approach frequently fails in FD- and MHF-EPR. Therefore, most studies of HS systems are performed on highly concentrated ground powder samples. Though, this approach can lead to inter-molecular couplings between neighboring complexes, partial ordering of the sample due to torquing [49] of the microcrystallites in the external magnetic field and deviations of the measured spectrum from a perfect powder pattern due to the polycrystalline nature of the samples [23]. Although, there is no easy way out of these challenges, measures can be taken to address them individually. Inter-molecular spin-spin interactions can be modulated even in polycrystalline powders by a gradual replacement of paramagnetic ions by diamagnetic equivalents. However, to perform the replacement such that the magnetic properties remain unaltered is a challenging task. Orientation of the sample in the magnetic field can be avoided by fixation of the powder in a matrix (e.g., in a pressed pellet of HDPE or Teflon) or by zero-field FD-EPR measurements. The latter are also less prone to artifacts arising from imperfect powder averaging in polycrystalline samples.

Further deviations between experiment and simulation may originate from the assumptions made in the computer simulations. Generally, terms up to the order $2S$ in the spin operator \hat{S} are effective in the SH [53]. Hence, with increasing S the complexity of the SH increases. Since the disentanglement of all contributing magnetic parameter is rarely possible, more cursory effective models are used. Validation of these models requires a variation of the experimental parameters over a very wide range and a comparison of data sets obtained on different spectrometers. However, even in cases where the dominating SH terms are identified, the simulation of HS spectra can be tricky. For instance, simulated field-domain EPR spectra of HS systems with looping transitions critically depend on the starting field [32]. The choice of a too coarse powder-averaging grid can lead to severe artifacts. Comparison of field-domain and zero-field FD-EPR data can again help to improve the situation.

Finally, instrumental peculiarities have to be considered. The realization of very wide frequency- and/or field-sweeps is difficult.

Uncertainties in the experimental parameters, which are very well controlled in state-of-the-art single- (conventional) frequency spectrometers, can therefore impair the precision of broadband EPR measurements. Relevant issues include: phase variations due to source instabilities, long-term variations and standing waves in the transmission lines, limited knowledge of the incident excitation power and thereby the saturation behavior of the sample under study, and inaccurate B_0 calibration. Solutions to these challenges strongly depend on the employed spectrometer concept and are part of the ongoing progress in high-frequency EPR-spectrometer development.

These developments are challenging, and as a result, EPR spectrometers covering a very broad excitation-energy/magnetic-field range are still much less available than, e.g., X- and Q-band spectrometers. In fact, most broadband EPR spectrometers are unique. Hence, studies in the SH parameters of many HS systems were limited to a single EPR spectrometer. However, it is our strong belief that the availability of an increasing number of broadband EPR spectrometers (including user facilities) [54] and simulation capabilities, will lead to a systematic discrimination between sample-related, theoretical and instrumental influences on the EPR spectra of HS states with very large ZFS. Such studies will further increase the information content extractable from the EPR spectra.

6. Outlook

In the preceding sections of this article, we described the benefits and working principles of FD-FT THz-EPR based on THz-CSR, discussed FD-EPR simulation strategies and exemplified their combined use for studies in the spin-coupling parameters of mono- and multinuclear HS systems with very large ZFS. However, the potential of this approach is far from being fully exploited.

FD-FT THz-EPR is the ideal technique to study EPR transitions distributed over a very wide transition-energy range, which is very challenging or even impossible with other EPR techniques. For example, HS TMs like Ni^{II} [6] or Co^{II} [7] can exhibit ZFS far beyond 30 cm^{-1} . Even higher ZFS are found in lanthanides. Mono- and multinuclear complexes containing HS TMs or lanthanides, will therefore remain among the prime targets of such studies. Thereby, FD-FT THz-EPR can provide further highly-desired pieces of information, relevant for future magneto-structural correlation studies and the characterization of MNMs with ever larger magnetic anisotropies.

The recent increase of the experimental versatility and sensitivity of the FD-FT THz-EPR set-up arises from the insertion of quasi-optical components, which conserve the polarization of the THz-radiation. This allows now for free choice of the orientation between B_0 and B_1 as well as measurements in Voigt and Faraday configurations. This freedom can be employed to study, e.g., the parity of spin states involved in the EPR [27] and realize induction-mode detection schemes, which can potentially improve the detection sensitivity.

The further development of FD-FT THz-EPR will significantly benefit from the availability of higher and higher magnetic fields and novel excitation sources. In particular, the employment of accelerators as excitation sources for EPR experiments in the range between 3 cm^{-1} (W-band) and the THz and FIR range has only started [16,21,55,56]. Optimization of these sources will increase their stability and thereby the achievable signal to noise ratio in the measured EPR spectra.

In addition to its stable broadband high-power spectrum, THz-CSR offers another very promising characteristic, namely time dependence. THz-CSR consists of short high-power and high-repetition-rate (up to 500 MHz) pulses as it results from ps-long electron bunches in the storage ring. This radiation can be used

for transient THz spectroscopy [57] and potentially also for EPR experiments in time domain. The prospects of FD-FT THz-EPR may even rise by next-generation accelerator sources. In particular, the concept of a variable-pulse-length storage ring projected by Helmholtz-Zentrum Berlin (BESSY-VSR), will increase the achievable THz-CSR power levels, the variability in the choice of the excitation spectrum and the time structure of the emitted THz-pulses [58].

These achievements will enable novel FD-FT THz-EPR detection schemes for studies in the SH parameters of HS systems, which are currently out of reach due to low spin concentration, low availability or extreme ZFS.

Acknowledgment

We thank Joshua Telser (Roosevelt University, Chicago, IL, USA), Berta Martins and Holger Dobbek (Humboldt University, Berlin, Germany) and Dawid Pinkowicz (Jagiellonian University, Krakow) for providing samples, as well as Stefan Stoll (University of Washington, Seattle, WA, USA) and Jan Dreiser (Paul Scherrer Institut, Villigen, Switzerland) for their contribution to the development of FD-EPR simulation routines. In addition, we are grateful to all the collaborators and users of the THz-EPR user station at BESSY II, for their input to improve the set-up. Technical support by Dirk Ponwitz is gratefully acknowledged. This work was funded by the German Federal Ministry of Education and Research (BMBF, network project EPR-Solar) and Deutsche Forschungsgemeinschaft (DFG, SPP 1601 and research fellowship NE 2064/1-1 FOR to J.N.) and HZB's user program.

References

- [1] R. Boca, Zero-field splitting in metal complexes, *Coord. Chem. Rev.* 248 (2003) 757–815.
- [2] F. Neese, Zero-field splitting, in: M. Kaupp, M. Bühl, V.G. Malkin (Eds.), *Calculation of NMR and EPR Parameters. Theory and Applications*, Wiley-VCH, Weinheim, 2004, pp. 541–566.
- [3] F. Neese, E.I. Solomon, Interpretation and calculation of spin-hamiltonian parameters in transition metal complexes, in: J.S. Miller, M. Dillon (Eds.), *Magnetism: Molecules to Materials*, Wiley-VCH, Weinheim, 2003, pp. 345–466.
- [4] J.W. Sharples, D. Collison, E.J.L. McInnes, J. Schnack, E. Palacios, M. Evangelisti, Quantum signatures of a molecular nanomagnet in direct magnetocaloric measurements, *Nat. Commun.* 5 (2014) 5321.
- [5] D. Gatteschi, A.L. Barra, A. Caneschi, A. Cornia, R. Sessoli, L. Sorace, EPR of molecular nanomagnets, *Coord. Chem. Rev.* 250 (2006) 1514–1529.
- [6] K.E.R. Marriot, L. Bhaskaran, C. Wilson, M. Medarde, S.T. Ochsnein, S. Hill, M. Murrie, Pushing the limits of magnetic anisotropy in trigonal bipyramidal Ni (ii), *Chem. Sci.* 6 (2015) 6823–6828.
- [7] Y. Rechkemmer, F.D. Breitgoff, M. van der Meer, M. Atanasov, M. Hakl, M. Orlita, P. Neugebauer, F. Neese, B. Sarkar, J. van Slageren, A four-coordinate cobalt(II) single-ion magnet with coercivity and a very high energy barrier, *Nat. Commun.* 7 (2016).
- [8] P.L. Richards, W.S. Caughey, H. Eberspaecher, G. Feher, M. Malley, Determination of zero-field splitting of Fe^{3+} in several heme compounds, *J. Chem. Phys.* 47 (1967) 1187–1188.
- [9] G.C. Brakett, P.L. Richards, H.H. Wickman, Far infrared spectra of several $Fe(III)$ complexes with spin $S = 3/2$, *Chem. Phys. Lett.* 6 (1970) 75–78.
- [10] G.C. Brakett, P.L. Richards, W.S. Caughey, Far-infrared magnetic resonance in $Fe(III)$ and $Mn(III)$ porphyrins, myoglobin, hemoglobin, ferrichrome-A, and $Fe(III)$ dithiocarbamates, *J. Chem. Phys.* 54 (1971) 4383–4401.
- [11] R.R. Joyce, P.L. Richards, Far-infrared spectra of Al_2O_3 doped with Ti, V, and Cr, *Phys. Rev.* 179 (1969) 375.
- [12] P.M. Champion, A.J. Sievers, Far infrared magnetic-resonance of deoxyhemoglobin and deoxymyoglobin, *J. Chem. Phys.* 72 (1980) 1569–1582.
- [13] J.C. Hill, R.G. Wheeler, Far-infrared spectra of erbium, dysprosium, and samarium ethyl sulphate, *Phys. Rev.* 152 (1966) 482–494.
- [14] Y. Rechkemmer, F.D. Breitgoff, M. van der Meer, M. Atanasov, M. Hakl, M. Orlita, P. Neugebauer, F. Neese, B. Sarkar, J. van Slageren, A four-coordinate cobalt(II) single-ion magnet with coercivity and a very high energy barrier, *Nat. Commun.* 7 (2016) 10467.
- [15] K. Ray, A. Begum, T. Weyhermüller, S. Piligkos, J. van Slageren, F. Neese, K. Wieghardt, The electronic structure of the isoelectronic, square-planar complexes $[Fe(L)_2]^{2-}$ and $[Co(LBu)_2]^{2-}$ ($L = L_2$ and $L = L_2$ = Benzene-1,2-dithiolates): an experimental and density functional theoretical study, *J. Am. Chem. Soc.* 127 (2005) 4403–4415.

- [16] L. Mihály, D. Talbayev, L.F. Kiss, J. Zhou, T. Fehér, A. Jánossy, Field-frequency mapping of the electron spin resonance in the paramagnetic and antiferromagnetic states of LaMnO_3 , *Phys. Rev. B* 69 (2004) 024414.
- [17] D. Talbayev, L. Mihály, J. Zhou, Antiferromagnetic resonance in LaMnO_3 at low temperature, *Phys. Rev. Lett.* 93 (2004) 017202.
- [18] S. de Brion, C. Darie, M. Holzapfel, D. Talbayev, L. Mihály, F. Simon, A. Jánossy, G. Chouteau, Spin excitations in the antiferromagnet NaNiO_2 , *Phys. Rev. B* 75 (2007) 094402.
- [19] M. Abo-Bakr, J. Feikes, K. Holldack, P. Kuske, W.B. Peatman, U. Schade, G. Wüstefeld, H.W. Hübers, Brilliant, coherent far-infrared (THz) synchrotron radiation, *Phys. Rev. Lett.* 90 (2003) 094801.
- [20] G.L. Carr, M.C. Martin, W.R. McKinney, K. Jordan, G.R. Neil, G.P. Williams, High-power terahertz radiation from relativistic electrons, *Nature* 420 (2002) 153.
- [21] A. Schnegg, J. Behrends, K. Lips, R. Bittl, K. Holldack, Frequency domain Fourier transform THz-EPR on single molecule magnets using coherent synchrotron radiation, *Phys. Chem. Chem. Phys.* 11 (2009) 6820–6825.
- [22] K. Holldack, A. Schnegg, THz electron paramagnetic resonance/THz spectroscopy at BESSY II, *J. Large-scale Res. Fac. JLSRF* 2 (2016) 51.
- [23] A.P. Forshaw, J.M. Smith, A. Ozarowski, J. Krzystek, D. Smirnov, S.A. Zvyagin, T. D. Harris, H.I. Karunadasa, J.M. Zadrozny, A. Schnegg, K. Holldack, T.A. Jackson, A. Alamiri, D.M. Barnes, J. Telser, Low-spin hexacoordinate Mn(III): synthesis and spectroscopic investigation of homoleptic $\text{Tris}(\text{pyrazolyl})\text{borate}$ and $\text{Tris}(\text{carbene})\text{borate}$ complexes, *Inorg. Chem.* 52 (2013) 144–159.
- [24] J. Nehr Korn, B.M. Martins, K. Holldack, S. Stoll, H. Dobbek, R. Bittl, A. Schnegg, Three-field splittings in metHb and metMb with aquo and fluoro ligands: a FD-FTTHz-EPR study, *Mol. Phys.* 111 (2013) 2696–2707.
- [25] J. Nehr Korn, J. Telser, K. Holldack, S. Stoll, A. Schnegg, Simulating frequency-domain electron paramagnetic resonance: bridging the gap between experiment and magnetic parameters for high-spin transition-metal ion complexes, *J. Phys. Chem. B* 119 (2015) 13816–13824.
- [26] X. Feng, J.-L. Liu, K.S. Pedersen, J. Nehr Korn, A. Schnegg, K. Holldack, J. Bendix, M. Sigrist, H. Mutka, D. Samohvalov, D. Aguila, M.-L. Tong, J.R. Long, R. Clerac, Multifaceted magnetization dynamics in the mononuclear complex $[\text{ReIVCl}_4(\text{CN})_2]_2$, *Chem. Commun.* 52 (2016) 12905–12908.
- [27] J. Nehr Korn, A. Schnegg, K. Holldack, S. Stoll, General magnetic transition dipole moments for electron paramagnetic resonance, *Phys. Rev. Lett.* 114 (2015) 010801.
- [28] J. Dreiser, A. Schnegg, K. Holldack, K.S. Pedersen, M. Schau-Magnussen, J. Nehr Korn, P. Tregenna-Piggott, H. Mutka, H. Weihe, J. Bendix, O. Waldmann, Frequency-domain Fourier-transform terahertz spectroscopy of the single-molecule magnet $\text{NEt}_4\text{Mn-2(5-Brsalen)(2)(MeOH)(2)Cr(CN)(6)}$, *Chem.-Eur. J.* 17 (2011) 7492–7498.
- [29] K.S. Pedersen, J. Dreiser, J. Nehr Korn, M. Gysler, M. Schau-Magnussen, A. Schnegg, K. Holldack, R. Bittl, S. Piligkos, H. Weihe, P. Tregenna-Piggott, O. Waldmann, J. Bendix, A linear single-molecule magnet based on Ru(III)(CN)(6)_3 , *Chem. Commun.* 47 (2011) 6918–6920.
- [30] J. Dreiser, K.S. Pedersen, A. Schnegg, K. Holldack, J. Nehr Korn, M. Sigrist, P. Tregenna-Piggott, H. Mutka, H. Weihe, V.S. Mironov, J. Bendix, O. Waldmann, Three-axis anisotropic exchange coupling in the single-molecule magnets $\text{NEt}_4[\text{MnII}_2(5\text{-Brsalen})_2(\text{MeOH})_2\text{MIII(CN)(6)}]_2$ ($\text{M}=\text{Ru, Os}$), *Chem. – A Eur. J.* 19 (2013) 3693–3701.
- [31] D. Pinkowicz, H.I. Southerland, C. Avendaño, A. Prosvirnin, C. Sanders, W. Wernsdorfer, K.S. Pedersen, J. Dreiser, R. Clérac, J. Nehr Korn, G.G. Simeoni, A. Schnegg, K. Holldack, K.R. Dunbar, Cyanide single-molecule magnets exhibiting solvent dependent reversible “On” and “Off” exchange bias behavior, *J. Am. Chem. Soc.* 137 (2015) 14406–14422.
- [32] S. Stoll, A. Schweiger, EasySpin, a comprehensive software package for spectral simulation and analysis in EPR, *J. Magn. Reson.* 178 (2006) 42–55.
- [33] P.F. Goldsmith, Quasioptical Systems: Gaussian Beam Quasioptical Propagation and Applications, Wiley-IEEE Press, New York, 1997.
- [34] C.E. Greninger, Reflective device for polarization rotation, *Appl. Opt.* 27 (1988) 774–776.
- [35] J. van Slageren, S. Vongtragool, B. Gorshunov, A.A. Mukhin, N. Karl, J. Krzystek, J. Telser, A. Müller, C. Sangregorio, D. Gatteschi, M. Dressel, Frequency-domain magnetic resonance spectroscopy of molecular magnetic materials, *Phys. Chem. Chem. Phys.* 5 (2003) 3837.
- [36] HZB, HZB user access tool GATE, 2016.
- [37] J. van Slageren, S. Vongtragool, A. Mukhin, B. Gorshunov, M. Dressel, Terahertz Faraday effect in single molecule magnets, *Phys. Rev. B* 72 (2005).
- [38] A.-L. Barra, A. Gräslund, K.K. Andersson, The use of Very High Frequency EPR (VHF-EPR) in studies of radicals and metal sites in proteins and small inorganic models, in: O. Grinberg, L. Berliner (Eds.), Very High Frequency (VHF) ESR/EPR, Kluwer/Plenum Publishers, 2004, pp. 145–163.
- [39] N. Cox, M. Retegan, F. Neese, D.A. Pantazis, A. Boussac, W. Lubitz, Electronic structure of the oxygen-evolving complex in photosystem II prior to O–O bond formation, *Science* 345 (2014) 804–808.
- [40] A. Bencini, D. Gatteschi, EPR of Exchange Coupled Systems, Springer Verlag, Berlin, 1990.
- [41] A. Furrer, T. Strässle, J. Mesot, Neutron Scattering in Condensed Matter Physics, World Scientific, 2009.
- [42] A. Caneschi, D. Gatteschi, R. Sessoli, A.L. Barra, L.C. Brunel, M. Guillot, Alternating current susceptibility, high field magnetization, and millimeter band EPR evidence for a ground $S = 10$ state in $[\text{Mn}_{12}\text{O}_{12}(\text{CH}_3\text{COO})_{16}(\text{H}_2\text{O})_4] \cdot 2\text{CH}_3\text{COOH} \cdot 4\text{H}_2\text{O}$, *J. Am. Chem. Soc.* 113 (1991) 5873–5874.
- [43] M. Baker, S. Blundell, N. Domingo, S. Hill, Spectroscopy methods for molecular nanomagnets, in: S. Gao (Ed.), Molecular Nanomagnets and Related Phenomena, Springer, Berlin, Heidelberg, 2015, pp. 231–291.
- [44] J. Krzystek, J. Telser, Measuring giant anisotropy in paramagnetic transition metal complexes with relevance to single-ion magnetism, *Dalton Trans.* 45 (2016) 16751–16763.
- [45] J. van Slageren, New directions in electron paramagnetic resonance spectroscopy on molecular nanomagnets, in: M. Drescher, G. Jeschke (Eds.), EPR Spectroscopy, Springer, Berlin, Heidelberg, 2012, pp. 199–234.
- [46] J. Dreiser, O. Waldmann, C. Dobe, G. Carver, S.T. Ochsenbein, A. Sieber, H.U. Güdel, J. van Duijn, J. Taylor, A. Podlesnyak, Quantized antiferromagnetic spin waves in the molecular Heisenberg ring CsFe_8 , *Phys. Rev. B* 81 (2010) 024408.
- [47] P. Albores, L.D. Slep, L.M. Baraldo, R. Baggio, M.T. Garland, E. Rentschler, Crystal structure and electronic and magnetic properties of hexacyanoosmate(III), *Inorg. Chem.* 45 (2006) 2361–2363.
- [48] G. Mathies, S.D. Chatziefthimiou, D. Maganas, Y. Sanakis, S. Sottini, P. Kyritsis, E.J.J. Groenen, High-frequency EPR study of the high-spin FeII complex $\text{Fe}[(\text{SPPH}_2)_2\text{N}]_2$, *J. Magn. Reson.* 224 (2012) 94–100.
- [49] J. Telser, J. Krzystek, A. Ozarowski, High-frequency and high-field electron paramagnetic resonance (HF-EPR): a new spectroscopic tool for bioinorganic chemistry, *J. Biol. Inorg. Chem.* 19 (2014) 297–318.
- [50] B. Parks, J. Loomis, E. Rumberger, D.N. Hendrickson, G. Christou, Linewidth of single-photon transitions in Mn_{12} -acetate, *Phys. Rev. B* 64 (2001) 184426.
- [51] K. Kozuki, T. Nagashima, M. Hangyo, Measurement of electron paramagnetic resonance using terahertz time-domain spectroscopy, *Opt. Express* 19 (2011) 24950–24956.
- [52] G. Jeschke, Electron paramagnetic resonance: recent developments and trends, *Curr. Opin. Solid State Mater. Sci.* 7 (2003) 181–188.
- [53] D.G. McGavin, W.C. Tennant, J.A. Weil, High-spin Zeeman terms in the spin Hamiltonian, *J. Magn. Reson.* 87 (1990) 92–109.
- [54] J. Telser, A. Ozarowski, J. Krzystek, High-frequency and -field electron paramagnetic resonance of transition metal ion (d block) coordination complexes, in: B.C. Gilbert, M.J. Davies, D.M. Murphy (Eds.), Electron Paramagnetic Resonance, vol. 23, The Royal Society of Chemistry, 2013, pp. 209–263.
- [55] S. Takahashi, L.C. Brunel, D.T. Edwards, J. van Tol, G. Ramian, S. Han, M.S. Sherwin, Pulsed electron paramagnetic resonance spectroscopy powered by a free-electron laser, *Nature* 489 (2012) 409–413.
- [56] S.A. Zvyagin, M. Ozerov, E. Čížmár, D. Kamenskyi, S. Zherlitsyn, T. Herrmannsdörfer, J. Wosnitzer, R. Wünsch, W. Seidel, Terahertz-range free-electron laser electron spin resonance spectroscopy: techniques and applications in high magnetic fields, *Rev. Sci. Instr.* 80 (2009) 073102.
- [57] V. Bragaglia, A. Schnegg, R. Calarco, K. Holldack, Epitaxial $\text{Ge}_2\text{Sb}_2\text{Te}_5$ probed by single cycle THz pulses of coherent synchrotron radiation, *Appl. Phys. Lett.* 109 (2016) 141903.
- [58] A. Jankowiak, G. Wüstefeld, Low- α operation of BESSY II and future plans for an alternating bunch length scheme BESSYVSR, *Synchrotron Radiat. News* 26 (2013) 22–24.